ACS central science

http://pubs.acs.org/journal/acscii

Research Article

Defect Engineering of Ceria Nanocrystals for Enhanced Catalysis via a High-Entropy Oxide Strategy

Yifan Sun, Tao Wu, Zhenghong Bao, Jisue Moon, Zhennan Huang, Zitao Chen, Hao Chen, Meijia Li, Zhenzhen Yang, Miaofang Chi, Todd J. Toops, Zili Wu, De-en Jiang, Jue Liu,* and Sheng Dai*

Cite This: *ACS Cent. Sci.* 2022, 8, 1081−1090

Read Online

ACCESS | Metrics & More | Article Recommendations | Supporting Information

ABSTRACT: Introducing transition-metal components to ceria (CeO_2) is important to tailor the surface redox properties for a broad scope of applications. The emergence of high-entropy oxides (HEOs) has brought transformative opportunities for oxygen defect engineering in ceria yet has been hindered by the difficulty in controllably introducing transition metals to the bulk lattice of ceria. Here, we report the fabrication of ceria-based nanocrystals with surface-confined atomic HEO layers for enhanced catalysis. The increased covalency of the transition-metal−oxygen bonds at the HEO−CeO_2 interface promotes the formation of surface oxygen vacancies, enabling efficient oxygen activation and replenishment for enhanced CO oxidation capabilities. Understanding the structural heterogeneity involving bulk and surface oxygen defects in nanostructured HEOs provides useful insights into rational design of atomically precise metal oxides, whose increased compositional and structural complexities give rise to expanded functionalities.

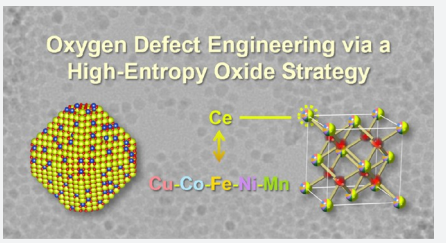

INTRODUCTION

Activation of lattice oxygen in ceria (CeO_2), usually associated with the formation and migration of oxygen vacancies, is fundamentally important for catalysis,[1] energy conversion,[2] magnetics,[3] sensing, and biomedical applications.[4,5] Introducing foreign metal species has been demonstrated to be an effective route to modulating the defect chemistry of ceria to access desirable properties.[6] First-row transition-metal elements, including Cu, Co, Fe, Ni, and Mn, are intriguing promoters to activate lattice oxygen in CeO_2 as substitutional dopant and/or interfacial domains.[7] In comparison with binary and ternary rare-earth oxides that are chemically inert, transition-metal substitution induces catalytically active centers that efficiently trigger a variety of molecular transformations.[8,9] For example, coordination-unsaturated copper species that are atomically dispersed on ceria yield high activity and stability for oxidation,[10] hydrogenation,[11] desulfurization,[12] and water-gas shift reactions,[13] as well as multiple electrocatalytic and photocatalytic reactions.[14,15]

The emergence of high-entropy oxides (HEOs) has introduced a distinct and transformative paradigm to manipulate the creation of oxygen defects in ceria-based oxides.[16] Different from high-entropy alloys (HEAs) with single-site occupancies, independent cation and anion sublattices in HEOs have greater structural tunabilities.[17−19] The enhanced configurational entropy gives rise to a higher endurance for lattice distortion. This allows the incorporation and stabilization of a higher concentration of aliovalent metal cations in the oxide lattice, which promotes the activation of lattice oxygen and formation of active species.[20] Additionally, the sluggish kinetics of HEOs introduced improved thermal and chemical stabilities for the metal species under reaction conditions.[21,22] The entropy-maximization principle has also been extended to the self-regeneration of the HEO-supported metal catalysts.[23,24]

Nonetheless, the applicability of this entropy-induced stabilization strategy is limited for ceria-based mixed oxides. The drastic size difference between the first-row transition metal and cerium atoms prompts the formation of oxide−oxide interfaces with inherent structural heterogeneities, which presents a fundamentally distinct scenario relative to the rare-earth-metal-based ceria solid solutions.[25] The associated influence on the oxygen defects of ceria has remained elusive, mainly due to the inherent complexities in oxygen-containing structures and difficulties in controllably creating and accurately identifying different types of oxygen defects. Various oxygen-deficient $CeO_{2-\delta}$ polymorphs within the Ce_2O_3−CeO_2 composition range can be formed upon oxygen loss.[6] Frenkel-type oxygen defects, which involve displacement of oxygen atoms from the octahedral interstitial sites in the fluorite lattice, are also common in CeO_2.[26] Discerning these stoichiometric and nonstoichiometric oxygen defects on the surface and in the bulk of ceria-based HEOs is thus challenging

Received: March 24, 2022
Published: June 16, 2022

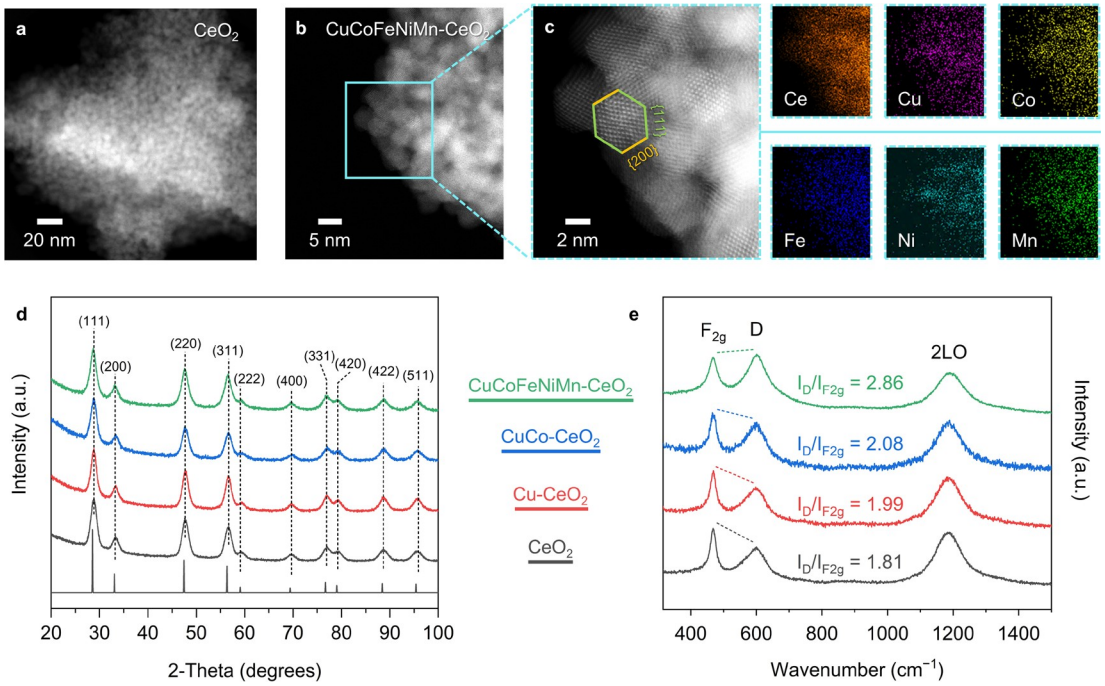

Figure 1. HAADF-STEM images of the annealed (a) CeO_2 and (b, c) CuCoFeNiMn-CeO_2 nanocrystals with EDS elemental maps showing a uniform distribution of the transition-metal elements. The terminated {111} and {200} facets in the truncated-octahedral shape are highlighted in green and yellow, respectively. (d) XRD patterns of the annealed transition-metal-substituted CeO_2 nanocrystals and the simulated reference pattern for comparison.[40] (e) UV Raman spectra of the annealed ceria-based samples with an excitation wavelength of 325 nm. The relative peak heights of F_{2g} and D are highlighted by dashed lines, with the intensity ratio ($I_D/I_{F_{2g}}$) estimated according to Lorentzian fitting.

yet crucial, particularly for nanocatalysis. Accessibility to surface oxygen defects determines the reaction pathways for low-temperature molecular conversions, whereas the pathways in the bulk favor oxygen transport for electrocatalysis and high-temperature thermocatalysis.[27,28] Fundamental insights are also desired to unveil and leverage the cation−oxygen-vacancy interactions in entropy-stabilized oxides for rational catalyst design.

Recent studies have observed pronounced local structural heterogeneities involving distinct surface and bulk domains of HEOs during synthesis and catalysis processes.[20] Instead of the formation of entropy-stabilized single-phase solid solutions,[29] building surface-confined HEO domains provides an alternative to tailor the surface reactivities of ceria via oxygen defect engineering. Here, we demonstrate the feasibility of constructing atomically thin HEO layers on ceria for enhanced catalysis. Neutron diffraction coupled with a pair-distribution function (PDF) analysis enables an atomistic investigation of the HEO−CeO_2 interface, which identifies both the intrinsic interstitial oxygen defects in the bulk lattice and the extrinsic oxygen vacancies on the surface of CeO_2. The strong covalency of the transition-metal−oxygen bonds facilitates the formation of surface-confined oxygen vacancies, which promotes efficient oxygen activation and replenishment for enhanced CO oxidation capabilities. Elucidating the structural heterogeneity involving surface and bulk oxygen defects in HEO nanocrystals lays the foundation for regulating oxygen defects in a broad range of complex oxides with expanded functionalities. For instance, controllably introducing different types of oxygen defects in nanoscale HEOs offers a potential entryway to modulating the electrochemical behaviors and engineering the oxide−oxide heterojunctions.

RESULTS AND DISCUSSION

Synthesis and Characterizations of Ceria-Based Nanocrystals. Ceria-based nanocrystals with tunable compositions were prepared using colloidal synthesis. During the synthesis, cerium and transition-metal oleates decompose in the mixture of octadecene and oleylamine at 220 °C and ultimately form metal oxide nanoparticles.[30] In addition to pristine CeO_2 nanoparticles, 5 atom % Cu-substituted CeO_2 (denoted Cu-CeO_2) and 5 atom % Cu- and 5 atom % Co-co-substituted CeO_2 (denoted CuCo-CeO_2), corresponding to binary copper−ceria and ternary copper−cobalt−ceria systems, respectively, were also fabricated.[10,31,32] Diversifying the dopant species can improve their dispersions on ceria.[33,34] Further extension to entropy-stabilized multicomponent oxides brings elevated transition-metal contents stabilized in the ceria lattice due to the enhanced entropic effects, as revealed by recent studies.[21,22,35] We thereby prepared CeO_2 simultaneously substituted with Cu, Co, Fe, Ni, and Mn (5 atom % for each element, denoted CuCoFeNiMn-CeO_2) to interrogate the entropic effects of the transition-metal promoters. Kinetic control in colloidal solutions warrants facile nucleation and growth of high-entropy nanocrystals at low temperatures,[36,37] where phase segregation would induce an enthalpic penalty. The surface-capped oleylamine ligands, which are absent for high-temperature solid-state materials, can be another factor that fine-tunes the formation pathway of the HEO nanocrystals.

As shown by the transmission electron microscopy (TEM) images with corresponding fast Fourier transform (FFT) patterns (Figures S1 and S2), the as-synthesized colloidal CeO_2 nanocrystallites are approximately 5 nm in size, with a truncated-octahedral shape exposing the {200} and {111} facets.[31,38] The ceria-based colloidal nanocrystals were then

https://doi.org/10.1021/acscentsci.2c00340
ACS Cent. Sci. 2022, 8, 1081−1090

annealed in air at 500 °C to remove the surface capping ligands for further characterization (Figure S3 and Tables S1 and S2). The high-angle annular dark-field scanning transmission electron microscopy (HAADF-STEM) images with the corresponding STEM-energy dispersive X-ray spectroscopy (EDS) element maps show that the annealed samples retain the truncated-octahedral morphology with uniform elemental distributions (Figure 1a–c). The annealed powders also become darker with elevated substitution levels, transitioning from pale yellow for CeO_2 to dark brown for CuCoFeNiMn-CeO_2 (Figure S4). This color transition can be ascribed to the decreased band gaps along with transition-metal incorporation, which extends the absorption edge to lower energies and may bring enhanced photocatalytic activities.[39]

Figure S5 and Figure 1d display the powder X-ray diffraction (XRD) data for the colloidal and annealed CeO_2, Cu-CeO_2, CuCo-CeO_2, and CuCoFeNiMn-CeO_2 samples, with a reference pattern for bulk CeO_2 for comparison.[40] Diffraction peaks corresponding to the CeO_2 phase can be identified for all of the samples, confirming retention of the host fluorite structure upon transition-metal incorporation. Notably, CuCoFeNiMn-CeO_2 only exhibits the characteristic diffraction peaks matching well with the fluorite structure of CeO_2, while additional crystalline peaks corresponding to the CuO phase emerge for the annealed copper-ceria sample with comparable transition-metal concentrations (~25 atom %) (Figure S6). This suggests that diversifying the transition-metal components mitigates the formation of the segregated transition-metal oxides in the bulk form. According to the Gibbs free energy equation ($\Delta G_{mix} = \Delta H_{mix} - T\Delta S_{mix}$), the enhanced configurational entropy (ΔS_{mix}) lowers the overall Gibbs free energy (ΔG_{mix}) through forming a homogeneous, randomly distributed phase,[41] which inhibits phase segregation and prompts better dispersions of the transition-metal species.

Figure 2e displays the ultraviolet (UV) Raman spectra of the annealed CeO_2 samples measured with a 325 nm excitation wavelength, which probes the dynamic interaction between the metal and oxygen atoms in ceria with a strong resonance effect.[42] CeO_2 exhibits the characteristic F_{2g} and defect-induced D modes at 467 and 599 cm^{-1}, respectively, together with the 2LO mode centered at 1188 cm^{-1}. In comparison, the D and 2LO modes of CuCoFeNiMn-CeO_2 exhibit an ~4 cm^{-1} red shift relative to those of the other samples, while the F_{2g} mode remains unchanged at ~467 cm^{-1}, implying substitution-induced modulation of the fluorite lattice (Table S3). Moreover, the relative intensity ratio between the D and F_{2g} modes ($I_D/I_{F_{2g}}$), which is indicative of the oxygen defect concentration in ceria,[43] increases from CeO_2 to CuCoFeNiMn-CeO_2. Concentration of the oxygen defects in ceria is thus positively correlated with the overall concentration of the transition-metal substituents. This is further supported by the Raman spectra with 532 nm excitation wavelength, as the D mode of CuCoFeNiMn-CeO_2 is observably stronger than those of the other samples (Figure S7 and Table S4).

Atomistic Insights into Oxygen Defects in Ceria-Based HEO Nanocrystals. The above results show the capability to create and modify oxygen defects in CeO_2 nanocrystals by introducing transition-metal substituents and cosubstituents. However, the long-range, macroscopic characteristics derived from the XRD pattern and Raman spectra can hardly be utilized to precisely pinpoint the origin of the observed structure difference, especially for nanoscale materials.[44] Possessing much smaller sizes in compariosn with that of cerium, the transition-metal substituents induce severe local distortions with short-range, nonperiodic features that underpin the local structures and the correlated functional properties.[45] In our case, the pronounced surface-dependent properties derived from the high surface-area-to-volume ratio of nanocrystals affords the opportunity to differentiate bulk and surface characteristics. We resorted to synchrotron- and neutron-based techniques to elucidate the nature, type, and concentration of the oxygen defects, which helps identify the metal–oxygen correlations in the ceria-based nanocrystals.

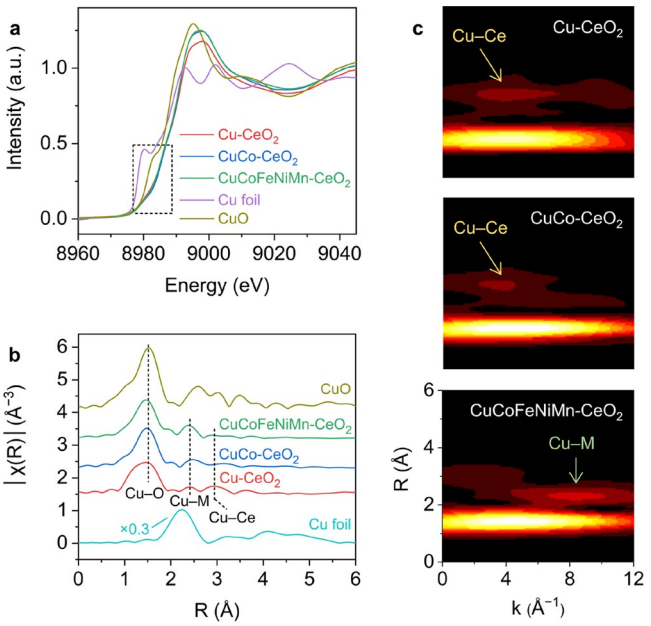

Figure 2. (a) Normalized Cu K-edge XANES spectra of the ceria-based samples with Cu and CuO references, with the pre-edge region (~8980 eV) being highlighted. (b) Cu K-edge EXAFS spectra of the ceria-based samples with Cu and CuO references. The peaks corresponding to Cu–O, Cu–M, and Cu–Ce shells are highlighted for comparison. (c) Wavelet transforms of EXAFS for Cu-CeO_2, CuCo-CeO_2, and CuCoFeNiMn-CeO_2.

X-ray absorption spectroscopy (XAS) was used to study the chemical environments of the metal cations. The Ce L_{III} edge remains almost identical for all the samples (Figure S8), indicating that the bulk Ce^{3+}/Ce^{4+} ratio remains unaltered upon transition-metal substitution. This is consistent with the unchanged surface Ce^{3+}/Ce^{4+} ratio as supported by the X-ray photoelectron spectroscopy (XPS) results of the Ce 3d region (Figure S9). We then focused on Cu, which is involved in all the three substituted samples, to acquire energetic insights. Figure 2a displays the Cu K-edge XANES spectra. The measurably higher absorption energy (E_0) values for Cu-CeO_2 (8991.5 eV), CuCo-CeO_2 (8991.6 eV), and CuCoFeNiMn-CeO_2 (8991.2 eV) relative to that for CuO (8990.3 eV) and the pre-edge features corresponding to the 1s → 3d transitions collectively indicate the existence of Cu^{2+}.[10] A previous study has attributed the oddly positive energy shift of Cu to the emergence of Cu^{3+} species,[31] while Lancaster and colleagues recently suggested that the strong covalency of the Cu–ligand bonding could be the main trigger.[46] For pristine CeO_2, the empty Ce 4f and filled O 2p energy levels, which are above and below the Fermi level, respectively, are the main contributors to the covalent interactions.[47] Incorporating Cu and other first-row transition-metal cosubstituents alters the hybridization and

https://doi.org/10.1021/acscentsci.2c00340
ACS Cent. Sci. 2022, 8, 1081–1090

energy level of the Ce and O orbitals, which will be discussed later.

The local coordination geometries of Cu were analyzed by fitting their Fourier-transformed extended X-ray absorption fine structure (EXAFS) spectra (Figure 2b and Figure S10 and Table S5). Cu-CeO_2, CuCo-CeO_2, and CuCoFeNiMn-CeO_2 all possessed the main Cu−O shell at ∼1.9 Å with reduced magnititude and a lower Cu coordination number (CN) of ∼2−3, reflecting the existence of transition-metal oxide motifs with small domains. Cu-CeO_2 also exhibited a minor Cu−Ce contribution at 3.26 Å (CN ≈ 3.0), which is attributed to the Cu−[O_x]−Ce structure with strong copper−ceria interactions.[48] Further wavelet transforms suggest that the Cu−Ce contribution weakens with an increased amount of the transition-metal substituents, while an additional coordination shell emerges at lower R and higher k values (Figure 2c). It is challenging to unambiguously identify the atoms giving rise to each individual scattering path, especially in the case of high-entropy CuCoFeNiMn-CeO_2, where different transition-metal atoms share similar weight numbers. On the basis of the copper−ceria interfacial perimeter model,[13] we tentatively assign this additional shell as the Cu−Cu distance (or Cu−M, where M represents Co, Fe, Ni, or Mn). XANES and EXAFS analyses together reveal that the atomically dispersed transition-metal substituents are strongly coordinated with the ligand oxygen from the CeO_2 domain.

Neutron diffraction, which relies on short-range nuclear interactions and thus possesses a high detection sensitivity for light elements,[49] was employed to identify the positions of the oxygen atoms in the transition-metal-substituted CeO_2 nanocrystals. According to the Rietveld refinements (Figures S11−S14 and Table S6), no (crystalline) impurity phase was observed for CeO_2, Cu-CeO_2, and CuCo-CeO_2, whereas a minor rock salt, sub-nanometer (<5 Å) HEO phase emerged for CuCoFeNiMn-CeO_2.[50] Moreover, no substantial changes were observed for the refined lattice parameters of CeO_2 among these four samples. This affords direct and unambiguous evidence showing the atomic-level structural heterogeneity, where the transition-metal substituents reside on the CeO_2 surface. Lattice shrinkage would be expected if Ce^{4+} (Ce^{3+}) in the bulk lattice were replaced by the transition-metal cations with smaller sizes. In addition, the surface enrichment of Ce^{3+} was also observed in the STEM-electron energy loss spectroscopy (EELS) analysis, as evidenced by the appearance of low-energy features at the Ce $M_{4,5}$ edge (Figure S15). Taken together, these results point to a structural picture where the substituted metal cations are embedded on the surface lattice of ceria, which constructs atomically thin HEO layers in CuCoFeNiMn-CeO_2.

The unexpected local structural disorder and interfacial effects between ultrasmall domains, which can hardly be detected using conventional techniques, play decisive roles in regulating the surface properties of high-entropy materials.[51,52] PDF analysis was applied to interpret this surface-confined transition-metal−ceria interface on the basis of the neutron diffraction data. Different from Rietveld refinements that focus on Bragg diffraction peaks, PDF analysis utilizes both Bragg scattering and diffuse scattering information and thereby possesses high sensitivities to short- and intermediate-range structures in nanoscale and amorphous systems.[53−56] As exhibited in Figure 3a, the first negative $G(r)$ peak at around 0.96−1.0 Å is assigned to the surface-attached O−H bonds, given the negative coherent nuclear scattering length of

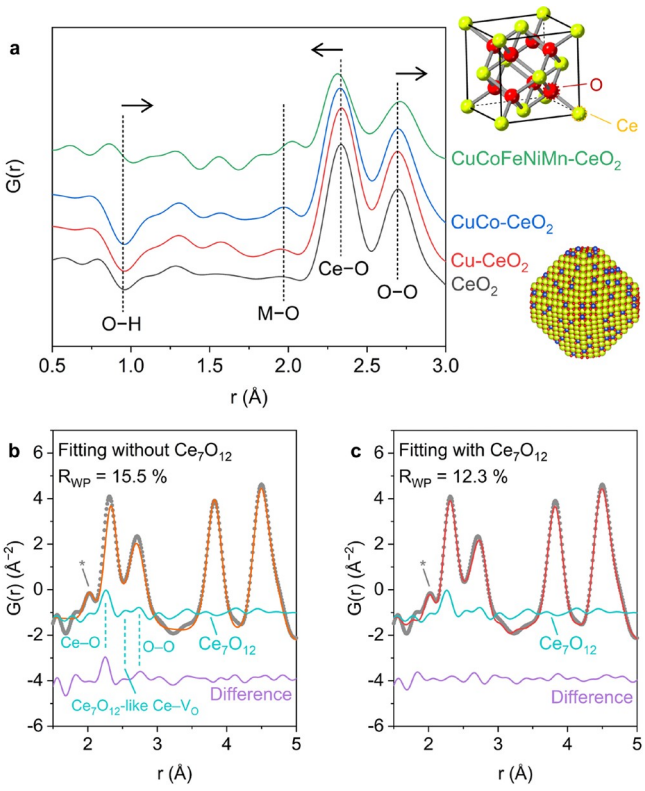

Figure 3. (a) Short-range neutron diffraction data for the transition-metal-substituted CeO_2 samples. The peaks corresponding to the O−H, M−O, Ce−O, and O−O correlations are noted for comparison. Insets showing the structure model of the fluorite structure of CeO_2 and illustrative model of the surface-substituted CeO_2 nanocrystals are provided at the top and bottom, respectively. Short-range PDF analysis of CuCoFeNiMn-CeO_2 (b) excluding and (c) including the Ce_7O_{12} phase. The contribution from the rock salt HEO domains, which is less than 5 Å as shown in Figure S21, is highlighted using an asterisk.

hydrogen. The peak at ∼1.95 Å is attributed to the nearest transition-metal−oxygen (M−O) correlation, which splits from a single peak to multiple deconvoluted peaks for CuCoFeNiMn-CeO_2 that correspond to different M−O bond lengths. This manifests the structure disorder in the surface-confined HEO layers. The nearest Ce−O and O−O correlations are located at ∼2.35 and ∼2.70 Å, respectively. Frenkel-type oxygen defects, which are common in the bulk lattice of CeO_2 due to the displacement of the oxygen anions along the ⟨111⟩ or ⟨110⟩ directions,[26] were introduced to the structure model for a short-range PDF analysis (Figures S16−S18). The concentrations of the interstitial oxygen defects were refined to be 9.3%, 12.0%, 13.6%, and 13.1% for CeO_2, Cu-CeO_2, CuCo-CeO_2 and CuCoFeNiMn-CeO_2, respectively (Table S7). The concentration of the intrinsic interstitial oxygen defects in the bulk lattice thus remains almost unaltered, due to the comparable sizes and morphologies of the ceria-based nanocrystals. Variation of the transition-metal substituents and cosubstituents situated on the CeO_2 surface thus has a negligible influence on the formation of oxygen defects deep within the bulk lattice.

Interestingly, the nearest Ce−O bond becomes shorter with transition-metal substitution, while the nearest O−O distance shifts toward higher r values (Figure 3a). This shift becomes non-negligible for CuCoFeNiMn-CeO_2 and results in a

https://doi.org/10.1021/acscentsci.2c00340
ACS Cent. Sci. 2022, 8, 1081−1090

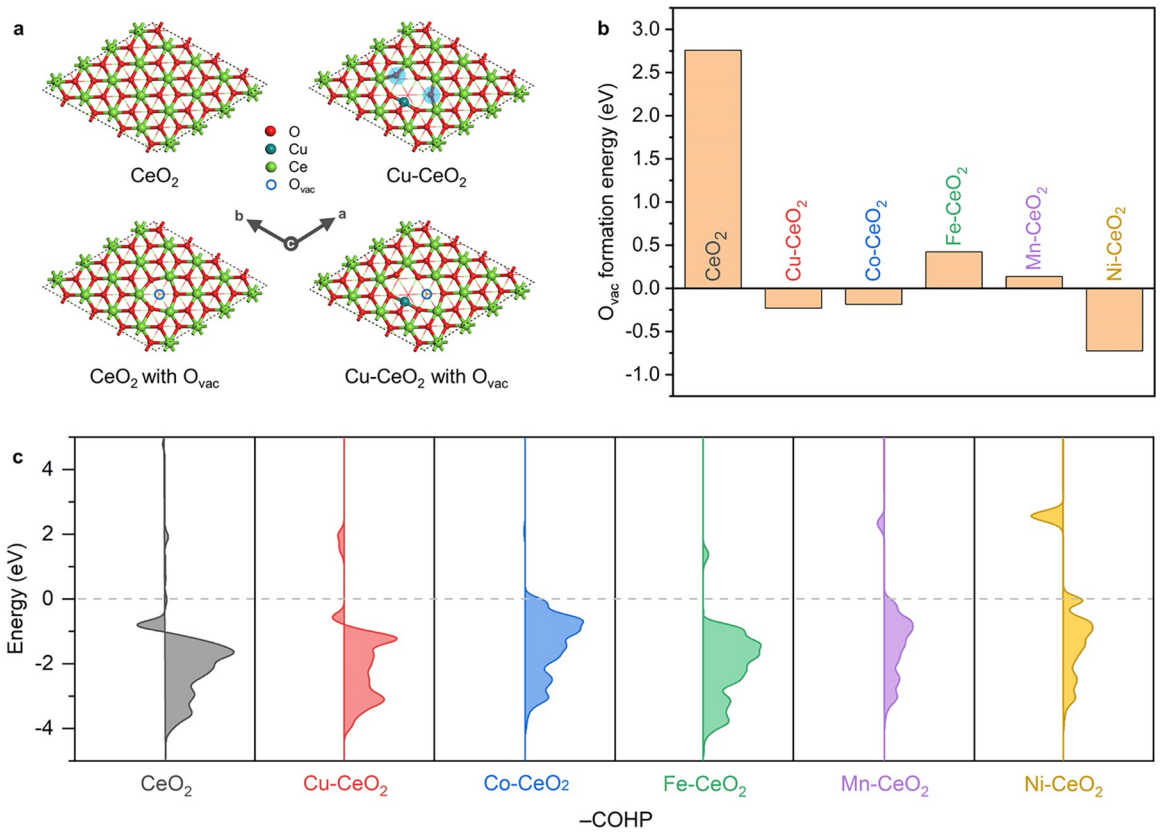

Figure 4. (a) Optimized surface structures of CeO_2-(111) and Cu-CeO_2-(111) with and without oxygen vacancies. (b) Calculated oxygen vacancy formation energies (E_{vac}) of the pristine and transition-metal-substituted CeO_2-(111). (c) Calculated COHP between the cerium and oxygen atoms on the surfaces of the pristine and transition-metal-substituted CeO_2-(111). The colored areas on the left and right correspond to the antibonding and bonding orbitals, respectively, and the Fermi level is noted using a dashed gray line.

discrepancy between the experimental and fitting results (Figure 3b). As the average fluorite structure model still well describes the intermediate-range PDF data above 5 Å (Figures S19 and S20), this opposite trend for the shift of the nearest Ce−O and O−O distances indicates an abundance of the surface oxygen defects in the HEO layers that drastically differ from the interstitial defects in the bulk fluorite lattice. Due to the small domain size, a large portion of the surface oxygen atoms from the CeO_2 domain are directly bonded to the transition-metal cations, resulting in pronounced surface-dependent phenomena for the high-entropy CuCoFeNiMn-CeO_2 sample.

To corroborate this hypothesis, we selected C−$Ce_2O_{3+\delta}$, Ce_7O_{12}, and $Ce_{11}O_{20}$, three common CeO_{2-x} polymorphs with different types of oxygen vacancies,[40] as an additional surface phase to the short-range PDF analysis of CuCoFeNiMn-CeO_2. The Ce_7O_{12} phase, a rhombohedral structure with periodic arrangements of oxygen vacancies perpendicular to the {111} planes,[57] was identified as the one that best describes the oxygen sublattice at the HEO−ceria interface. As displayed in Figure 3b, the difference between the simulated and experimental curves show three features in the range of 2−3 Å, which match well with the Ce−O, Ce_7O_{12}-like Ce−V_O (partially vacant oxygen sites), and Ce−O correlations in the Ce_7O_{12} structure, respectively. The PDF fitting for the CuCoFeNiMn-CeO_2 data including the Ce_7O_{12} phase yields a noticeable improvement (Figure 3c and Figure S21), demonstrating enrichment of surface-confined, oxygen-deficient phases. Accordingly, we were able to estimate the concentration of the Ce_7O_{12}-like oxygen vacancies for CeO_2 (<1%), Cu-CeO_2 (3.0%), CuCo-CeO_2 (5.0%), and CuCoFeNiMn-CeO_2 (13.4%) (Table S8 and Figure S22). In contrast to the relatively constant concentration of the interstitial oxygen defects, significantly more surface-confined oxygen vacancies are produced along with the formation of surface-confined HEO atomic layers in CuCoFeNiMn-CeO_2. This also suggests two orthogonal strategies to modulate the amount of the bulk and surface oxygen defects in ceria. Tuning the geometric parameters such as size and exposed facet facilitates the modification of the intrinsic, interstitial oxygen defects in the bulk lattice, while modulating the transition-metal substituents enables engineering of the extrinsic, surface-confined oxygen vacancies.

Computational Investigation of Formation of the Surface Oxygen Vacancies of Ceria-Based Nanocrystals. The oxygen vacancy formation energy has been shown to be an important descriptor for the reactivity of lattice oxygen on oxide surfaces. We hypothesize that, when the surface-confined HEOs are formed in CuCoFeNiMn-CeO_2, oxygen vacancy formation in the CeO_2 surface becomes more favorable, leading to the Ce_7O_{12}-like Ce−V_O species. To test this hypothesis and elucidate the correlation between formation of the transition-metal−oxygen bond and modulation of surface oxygen vacancies, we performed density functional theory (DFT) calculations at the GGA+U level based on a simplified model for the transition-metal-functionalized CeO_2 surfaces, using the oxygen vacancy formation energy (E_{vac}) as a descriptor.

https://doi.org/10.1021/acscentsci.2c00340
ACS Cent. Sci. 2022, 8, 1081−1090

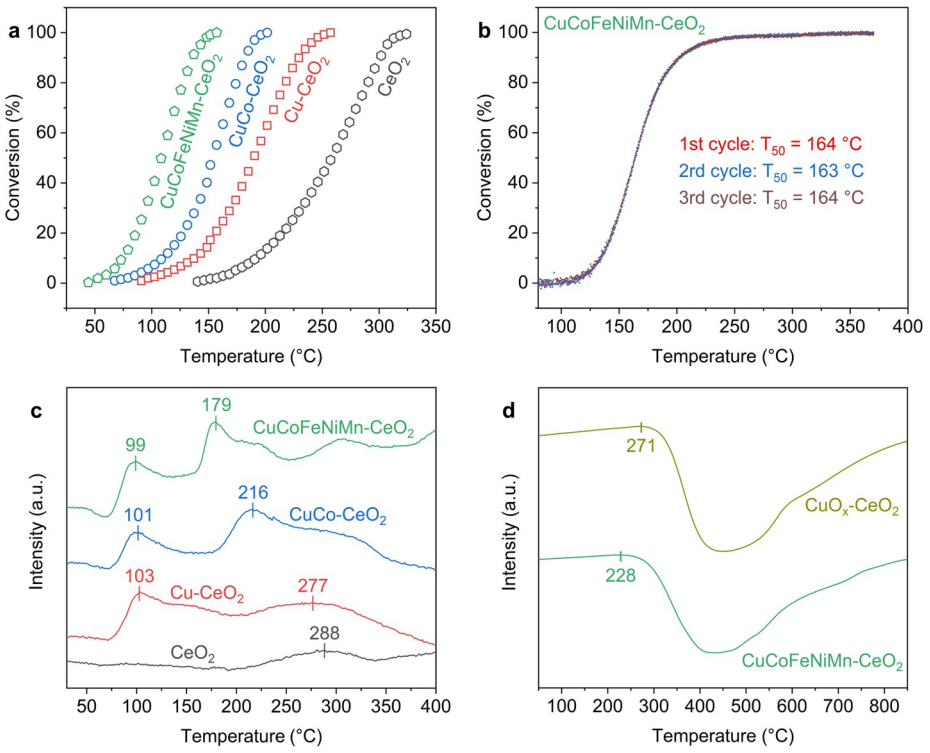

Figure 5. (a) CO oxidation light-off curves for the transition-metal-substituted CeO_2 samples, measured with 20 mg of the catalysts in 1% CO balanced with dry air at a flow rate of 12 mL min^{-1}. (b) CO oxidation light-off curves under simulated exhaust conditions (0.2% CO, 0.01% NO, 0.083% C_2H_4, 0.033% C_3H_6, 0.11% C_3H_8, 6.0% CO_2, 12.0% O_2, and 6.0% H_2O balanced with Ar) using the CuCoFeNiMn-CeO_2 catalyst for three repeated cycles, measured with 111 mg of the catalyst at a flow rate of 370 mL min^{-1} (GHSV ≈ 200000 h^{-1}). (c) CO-TPR profiles of the transition-metal-substituted CeO_2 catalysts with the CO consumption amount being highlighted. (d) Evolution of the $^{18}O_2$ species for CuCoFeNiMn-CeO_2 and CuO_x-CeO_2 during the TPOIE measurement, where the onset temperature is noted for comparison.

Because the truncated-octahedral shape of the ceria-based nanocrystals prominently exposes the {111} facet of CeO_2 (Figure 1), we use the (111) surface structure of CeO_2 as our starting model to probe how a surface substitutional doping by a 3d metal changes E_{vac} (Figure 4a).[58] One can see from Figure 4b that the E_{vac} value of M-CeO_2-(111) is much lower than that of the pristine CeO_2-(111) for M = Cu, Co, Fe, Mn, Ni. The key reason is that substitution of M for Ce on the surface creates 2-fold-coordinated oxygen atoms (Figure 4a and Figure S23), which are more active than the 3-fold-coordinated oxygens on the pristine CeO_2-(111). The negative E_{vac} values, especially for Ni-CeO_2-(111), indicate the favorable thermodynamic driving force for creating surface oxygen vacancies. The sluggish diffusion kinetics that are characteristic of HEOs[59] may further enhance the availability of the oxygen vacancies.

Bader charge analysis was performed to elucidate the oxidation state in Cu-CeO_2, with Cu_2O and CuO as references. We found that Cu in Cu-CeO_2 is slightly more oxidized in comparison to Cu in CuO (Figure S24), consistent with the observed positive energy shift of the Cu K-edge XANES spectra for Cu-CeO_2 (Figure 2a). We further investigated the change in the surface Ce−O bonding with M, using a crystal orbital Hamilton population (COHP) analysis (Figure 4c). One can see that the antibonding states of the CeO_2-(111) surface are either decreasing or pushed to above the Fermi level after substitutional doping by M. In other words, the Ce−O bonds are more strengthened in M-CeO_2 than in CeO_2. The computational results suggest that the formation of surface oxygen vacancies is thermodynamically favored in the high-entropy ceria nanocrystals. In comparison with Ce^{3+}/Ce^{4+}, the transition-metal cations possess lower oxidation states and smaller ionic radii, resulting in structural heterogeneities at the transition-metal−ceria interface. The strong bond covalency redistributes the charge on lattice oxygen and facilitates generation of the oxygen vacancies on the CeO_2 surface/subsurface instead of the interstitial vacancies in the bulk.

CO Oxidation Performance of Ceria-Based Nanocrystals. The surface oxygen vacancies induced by transition-metal substitution not only facilitate removal of oxygen atoms but also promote refilling of the vacant sites by adsorbed oxygen species. CO oxidation, a key technological process to treat automotive exhaust streams,[60,61] was selected as a model reaction to study the associated redox properties. The "light-off" curves show that introducing transition-metal species lowers the onset and complete conversion temperatures for CO oxidation (Figure 5a). The T_{50} values, the temperatures at which 50% of CO is converted to CO_2, are 257, 190, 155, and 109 °C for CeO_2, Cu-CeO_2, CuCo-CeO_2, and CuCoFeNiMn-CeO_2, respectively. The steady-state measurements at 80 °C show the same trend (Figure S25a). Following the Mars−van Krevelen mechanism,[34] CO molecules are adsorbed and oxidized by the activated lattice oxygen on the CeO_2 surface, where the accompanying oxygen vacancies are repeatedly filled by the dissociated oxygen molecules in the atmosphere. Notably, the CO oxidation activity is positively correlated with the concentration of the Ce_7O_{12}-like surface oxygen vacancies in the transition-metal-substituted CeO_2 nanocrystals. The apparent activation energies were calculated in the range of 48.6−66.8 kJ/mol (Figure S25b), consistent with previously

https://doi.org/10.1021/acscentsci.2c00340
ACS Cent. Sci. 2022, 8, 1081−1090

reported values.[8] This also validates that the activity difference originates from the different amounts of active sites that share the same Mars–van Krevelen mechanism. We further applied the optimal CuCoFeNiMn-CeO_2 catalyst to the treatment of exhaust streams, which showed compelling catalytic activity and stability under harsh conditions (GHSV ≈ 200000 h^{-1}), as displayed in Figure 5b and Figure S26. Inherent compositional diversities in HEOs afford separate active metal sites for adsorption and conversion of competing reactant molecules, which include CO, CO_2, hydrocarbons, NO_x, and H_2O in the exhaust streams. This points out a new direction for the design of CeO_2-based noble-metal-free catalysts for enhanced catalysis, where relevant studies have mainly focused on improving the CO oxidation activity or the performance of preferential oxidation of CO in excess hydrogen (PROX).[8,10,31,33,48] In addition to the catalytic activity, the sluggish kinetics of HEOs may reinforce the resistance to hydrocarbon inhibitions and catalyst stability during long-term operations, both of which are pivotal for industrial exhaust treatments.

CO temperature-programmed reduction (CO-TPR) was conducted to evaluate the reducibility of the transition-metal-substituted CeO_2 nanocrystals. As shown in Figure 5c, Cu-CeO_2 exhibits two peaks at 103 and 277 °C, corresponding to the reduction of the CuO_x clusters weakly bound to CeO_2 and the Cu–[O_x]–Ce structure with strong covalent copper–ceria interactions, respectively.[48] While the position of the first peak remains at ∼100 °C, the second peak observably shifts toward lower temperatures for CuCo-CeO_2 (216 °C) and CuCoFeNiMn-CeO_2 (179 °C). This suggests that the incorporation of the additional transition-metal species other than Cu facilitates reduction of the M–[O_x]–Ce structures, allowing activation and utilization of surface lattice oxygen at lower temperatures. In parallel, the CO consumption amount also increases from Cu-CeO_2 (256 μmol g^{-1}) and CuCo-CeO_2 (294 μmol g^{-1}) to CuCoFeNiMn-CeO_2 (562 μmol g^{-1}), highlighting the enlargement of the HEO–CeO_2 heterointerface for CO activation. A similar trend was observed for the H_2-TPR data (Figure S25c), whereas differentiation of the different reduction peaks became challenging, presumably due to the stronger reducing ability of H_2 in comparison with that of CO. In light of the above experimental and computational studies, we infer that the strong covalency of the M–O bonds in the M–[O_x]–Ce structures leads to the formation and stabilization of surface oxygen vacancies. With maximized active sites, the constructed HEO layers on ceria enable efficient oxygen activation and replenishment for enhanced CO conversions.

To unveil the entropic effects in oxygen defect formation and correlated lattice oxygen activation, we applied temperature-programmed oxygen isotope exchange (TPOIE) to compare the oxygen exchange behaviors of the high-entropy oxide (CuCoFeNiMn-CeO_2) and binary oxide (CuO_x-CeO_2) with comparable transition-metal concentrations (Table S2).[62] As shown in Figure 5d, the consumption of $^{18}O_2$ started at 228 °C for CuCoFeNiMn-CeO_2, observably lower than that for CuO_x-CeO_2 (271 °C). A similar trend was observed for the evolution of the $^{16}O_2$ and $^{16}O^{18}O$ signals (Figure S27), which demonstrates the enhanced oxygen exchange capability for CuCoFeNiMn-CeO_2 relative to that for CuO_x-CeO_2. Meanwhile, the normalized oxygen capacity for CuCoFeNiMn-CeO_2 is around the same (104%) as that for CuO_x-CeO_2. The TPOIE results indicate that the surface-confined atomic HEO layers enriched with Ce_7O_{12}-like oxygen vacancies facilitate the exchange between gas-phase oxygen and surface lattice oxygen of CeO_2. The enhanced configurational entropy affords a distinct route to activating surface lattice oxygen, benefiting the formation, migration, and utilization of active oxygen species for oxidation reactions. This brings opportunities to tackle issues that are considered challenging for conventional mixed-oxide catalysts.

CONCLUSIONS

Given the broad scope of potential applications for ceria-based nanomaterials, it is pivotal to tailor the oxygen defects in CeO_2 through a rational structure and composition design. As a distinct strategy to tune the oxygen defects in ceria, entropy stabilization has been mostly limited to single-phase solid solutions. Here, we demonstrate that the surface-confined HEO atomic layers, where different transition metals are randomly embedded and stabilized on the surface lattice of ceria, have profound effects on the creation of oxygen defects. The formation of the bulk interstitial oxygen defects is dependent on the size and geometry of the ceria nanocrystals, whereas tuning of the cluster surface defects relies on the transition-metal–CeO_2 interface engineering. With enhanced bond covalency and maximized active sites, the CuCoFeNiMn-CeO_2 sample exhibits optimal CO oxidation capabilities. These atomistic insights into the surface and bulk structures of ceria-based HEO nanocrystals have important implications for oxygen defect engineering in reducible metal oxides.[63] For example, the ability to control the surface and bulk oxygen defects of nanoscale HEOs is important in the exploration of new topological materials, where the interior electronic and magnetic properties are completely different from those on the surface or at the oxide–oxide interface.[64] More work is anticipated to unravel the metal–oxygen covalency in mixed and entropy-stabilized metal oxides, as the atomic-scale structural heterogeneities may benefit lattice oxygen activation for catalytic and sensing applications.

ASSOCIATED CONTENT

Supporting Information

The Supporting Information is available free of charge at https://pubs.acs.org/doi/10.1021/acscentsci.2c00340.

Additional experimental and calculation details and additional figures and tables as described in the text (PDF)

AUTHOR INFORMATION

Corresponding Authors

Sheng Dai – *Chemical Sciences Division, Oak Ridge National Laboratory, Oak Ridge, Tennessee 37831, United States; Department of Chemistry, The University of Tennessee, Knoxville, Tennessee 37996, United States;* orcid.org/0000-0002-8046-3931; Email: dais@ornl.gov

Jue Liu – *Neutron Scattering Division, Oak Ridge National Laboratory, Oak Ridge, Tennessee 37831, United States;* orcid.org/0000-0002-4453-910X; Email: liuj1@ornl.gov

Authors

Yifan Sun – *Chemical Sciences Division, Oak Ridge National Laboratory, Oak Ridge, Tennessee 37831, United States; Frontiers Science Center for Transformative Molecules, School of Chemistry and Chemical Engineering, Shanghai Jiao Tong*

https://doi.org/10.1021/acscentsci.2c00340
ACS Cent. Sci. 2022, 8, 1081–1090

University, Shanghai 200240, China; orcid.org/0000-0002-4082-5379

Tao Wu − *Department of Chemistry, University of California, Riverside, California 92521, United States*

Zhenghong Bao − *Chemical Sciences Division, Oak Ridge National Laboratory, Oak Ridge, Tennessee 37831, United States*

Jisue Moon − *Chemical Sciences Division, Oak Ridge National Laboratory, Oak Ridge, Tennessee 37831, United States*

Zhennan Huang − *Center for Nanophase Materials Sciences, Oak Ridge National Laboratory, Oak Ridge, Tennessee 37831, United States*

Zitao Chen − *Center for Nanophase Materials Sciences, Oak Ridge National Laboratory, Oak Ridge, Tennessee 37831, United States;* orcid.org/0000-0002-6111-7750

Hao Chen − *Department of Chemistry, The University of Tennessee, Knoxville, Tennessee 37996, United States;* orcid.org/0000-0002-6658-4198

Meijia Li − *Chemical Sciences Division, Oak Ridge National Laboratory, Oak Ridge, Tennessee 37831, United States*

Zhenzhen Yang − *Chemical Sciences Division, Oak Ridge National Laboratory, Oak Ridge, Tennessee 37831, United States*

Miaofang Chi − *Center for Nanophase Materials Sciences, Oak Ridge National Laboratory, Oak Ridge, Tennessee 37831, United States;* orcid.org/0000-0003-0764-1567

Todd J. Toops − *Buildings and Transportation Science Division, Oak Ridge National Laboratory, Oak Ridge, Tennessee 37831, United States*

Zili Wu − *Chemical Sciences Division, Oak Ridge National Laboratory, Oak Ridge, Tennessee 37831, United States; Center for Nanophase Materials Sciences, Oak Ridge National Laboratory, Oak Ridge, Tennessee 37831, United States;* orcid.org/0000-0002-4468-3240

De-en Jiang − *Department of Chemistry, University of California, Riverside, California 92521, United States;* orcid.org/0000-0001-5167-0731

Complete contact information is available at: https://pubs.acs.org/10.1021/acscentsci.2c00340

Notes

The authors declare no competing financial interest.

■ ACKNOWLEDGMENTS

This work was supported by the U.S. Department of Energy (DOE), Office of Science, Office of Basic Energy Sciences, Chemical Sciences, Geosciences, and Biosciences Division, Catalysis Science Program. Use of the Advanced Photon Source was supported by the U.S. Department of Energy, Office of Science, Office of Basic Energy Sciences, under Contract No. DE-AC02-06CH11357. Neutron total scattering measurements were conducted at the NOMAD beamline at the Spallation Neutron Source, Oak Ridge National Laboratory, which was sponsored by the Scientific User Facilities Division, Office of Basic Sciences, U.S. Department of Energy. Part of the work including Raman and STEM was conducted at the Center for Nanophase Materials Sciences, which is a DOE Office of Science User Facility. We thank Yujia Bian for the assistance during XAS experiments at the 10-BM beamline at the Advanced Photon Source at Argonne National Laboratory and Harry M. Meyer III at Oak Ridge National Laboratory for XPS acquisition and analysis.

■ REFERENCES

(1) Trovarelli, A. Catalytic Properties of Ceria and CeO_2-Containing Materials. *Catal. Rev. - Sci. Eng.* **1996**, *38*, 439−520.

(2) Yang, C.; Wong, R. A.; Hong, M.; Yamanaka, K.; Ohta, T.; Byon, H. R. Unexpected Li_2O_2 Film Growth on Carbon Nanotube Electrodes with CeO_2 Nanoparticles in Li−O_2 Batteries. *Nano Lett.* **2016**, *16*, 2969−2974.

(3) Ackland, K.; Coey, J. M. D. Room Temperature Magnetism in CeO_2—A Review. *Phys. Rep.* **2018**, *746*, 1−39.

(4) Jasinski, P.; Suzuki, T.; Anderson, H. U. Nanocrystalline Undoped Ceria Oxygen Sensor. *Sens. Actuators, B* **2003**, *95*, 73−77.

(5) Han, S. I.; Lee, S.; Cho, M. G.; Yoo, J. M.; Oh, M. H.; Jeong, B.; Kim, D.; Park, O. K.; Kim, J.; Namkoong, E.; Jo, J.; Lee, N.; Lim, C.; Soh, M.; Sung, Y.-E.; Yoo, J.; Park, K.; Hyeon, T. Epitaxially Strained CeO_2/Mn_3O_4 Nanocrystals as an Enhanced Antioxidant for Radioprotection. *Adv. Mater.* **2020**, *32*, 2001566.

(6) Montini, T.; Melchionna, M.; Monai, M.; Fornasiero, P. Fundamentals and Catalytic Applications of CeO_2-Based Materials. *Chem. Rev.* **2016**, *116*, 5987−6041.

(7) Sun, Y.; Polo-Garzon, F.; Bao, Z.; Moon, J.; Huang, Z.; Chen, H.; Chen, Z.; Yang, Z.; Chi, M.; Wu, Z.; Liu, J.; Dai, S. Manipulating Copper Dispersion on Ceria for Enhanced Catalysis: A Nanocrystal-Based Atom-Trapping Strategy. *Adv. Sci.* **2022**, *9*, 2104749.

(8) Wang, W.-W.; Du, P.-P.; Zou, S.-H.; He, H.-Y.; Wang, R.-X.; Jin, Z.; Shi, S.; Huang, Y.-Y.; Si, R.; Song, Q.-S.; Jia, C.-J.; Yan, C.-H. Highly Dispersed Copper Oxide Clusters as Active Species in Copper-Ceria Catalyst for Preferential Oxidation of Carbon Monoxide. *ACS Catal.* **2015**, *5*, 2088−2099.

(9) Zhang, P.; Lu, H.; Zhou, Y.; Zhang, L.; Wu, Z.; Yang, S.; Shi, H.; Zhu, Q.; Chen, Y.; Dai, S. Mesoporous $MnCeO_x$ Solid Solutions for Low Temperature and Selective Oxidation of Hydrocarbons. *Nat. Commun.* **2015**, *6*, 8446.

(10) Yu, W.-Z.; Wang, W.-W.; Li, S.-Q.; Fu, X.-P.; Wang, X.; Wu, K.; Si, R.; Ma, C.; Jia, C.-J.; Yan, C.-H. Construction of Active Site in a Sintered Copper−Ceria Nanorod Catalyst. *J. Am. Chem. Soc.* **2019**, *141*, 17548−17557.

(11) Lin, L.; Yao, S.; Liu, Z.; Zhang, F.; Li, N.; Vovchok, D.; Martínez-Arias, A.; Castañeda, R.; Lin, J.; Senanayake, S. D.; Su, D.; Ma, D.; Rodriguez, J. A. In Situ Characterization of Cu/CeO_2 Nanocatalysts for CO_2 Hydrogenation: Morphological Effects of Nanostructured Ceria on the Catalytic Activity. *J. Phys. Chem. C* **2018**, *122*, 12934−12943.

(12) Li, Z.; Flytzani-Stephanopoulos, M. Cu−Cr−O and Cu−Ce−O Regenerable Oxide Sorbents for Hot Gas Desulfurization. *Ind. Eng. Chem. Res.* **1997**, *36*, 187−196.

(13) Chen, A.; Yu, X.; Zhou, Y.; Miao, S.; Li, Y.; Kuld, S.; Sehested, J.; Liu, J.; Aoki, T.; Hong, S.; Camellone, M. F.; Fabris, S.; Ning, J.; Jin, C.; Yang, C.; Nefedov, A.; Wöll, C.; Wang, Y.; Shen, W. Structure of the Catalytically Active Copper−Ceria Interfacial Perimeter. *Nat. Catal* **2019**, *2*, 334−341.

(14) Yang, K.; Li, D.-F.; Huang, W.-Q.; Xu, L.; Huang, G.-F.; Wen, S. Origin of Enhanced Visible-Light Photocatalytic Activity of Transition-Metal (Fe, Cr and Co)-Doped CeO_2: Effect of 3d Orbital Splitting. *Appl. Phys. A* **2017**, *123*, 96.

(15) Wang, Y.; Chen, Z.; Han, P.; Du, Y.; Gu, Z.; Xu, X.; Zheng, G. Single-Atomic Cu with Multiple Oxygen Vacancies on Ceria for Electrocatalytic CO_2 Reduction to CH_4. *ACS Catal.* **2018**, *8*, 7113−7119.

(16) Rost, C. M.; Sachet, E.; Borman, T.; Moballegh, A.; Dickey, E. C.; Hou, D.; Jones, J. L.; Curtarolo, S.; Maria, J.-P. Entropy-Stabilized Oxides. *Nat. Commun.* **2015**, *6*, 8485.

(17) Xin, Y.; Li, S.; Qian, Y.; Zhu, W.; Yuan, H.; Jiang, P.; Guo, R.; Wang, L. High-Entropy Alloys as a Platform for Catalysis: Progress, Challenges, and Opportunities. *ACS Catal.* **2020**, *10*, 11280−11306.

(18) Feng, D.; Dong, Y.; Zhang, L.; Ge, X.; Zhang, W.; Dai, S.; Qiao, Z. Holey Lamellar High-Entropy Oxide as an Ultra-High-Activity Heterogeneous Catalyst for Solvent-free Aerobic Oxidation of Benzyl Alcohol. *Angew. Chem. Int. Ed* **2020**, *59*, 19503−19509.

(19) Gu, K.; Wang, D.; Xie, C.; Wang, T.; Huang, G.; Liu, Y.; Zou, Y.; Tao, L.; Wang, S. Defect-Rich High-Entropy Oxide Nanosheets for Efficient 5-Hydroxymethylfurfural Electrooxidation. *Angew. Chem. Int. Ed.* **2021**, *60*, 20253−20258.
(20) Sun, Y.; Dai, S. High-Entropy Materials for Catalysis: A New Frontier. *Sci. Adv.* **2021**, *7*, No. eabg1600.
(21) Li, T.; Yao, Y.; Huang, Z.; Xie, P.; Liu, Z.; Yang, M.; Gao, J.; Zeng, K.; Brozena, A. H.; Pastel, G.; Jiao, M.; Dong, Q.; Dai, J.; Li, S.; Zong, H.; Chi, M.; Luo, J.; Mo, Y.; Wang, G.; Wang, C.; Shahbazian-Yassar, R.; Hu, L. Denary Oxide Nanoparticles as Highly Stable Catalysts for Methane Combustion. *Nat. Catal.* **2021**, *4*, 62−70.
(22) Xu, H.; Zhang, Z.; Liu, J.; Do-Thanh, C.-L.; Chen, H.; Xu, S.; Lin, Q.; Jiao, Y.; Wang, J.; Wang, Y.; Chen, Y.; Dai, S. Entropy-Stabilized Single-Atom Pd Catalysts via High-Entropy Fluorite Oxide Supports. *Nat. Commun.* **2020**, *11*, 3908.
(23) Hou, S.; Ma, X.; Shu, Y.; Bao, J.; Zhang, Q.; Chen, M.; Zhang, P.; Dai, S. Self-Regeneration of Supported Transition Metals by a High Entropy-Driven Principle. *Nat. Commun.* **2021**, *12*, 5917.
(24) Chen, H.; Sun, Y.; Yang, S.; Wang, H.; Dmowski, W.; Egami, T.; Dai, S. Self-Regenerative Noble Metal Catalysts Supported on High-Entropy Oxides. *Chem. Commun.* **2020**, *56*, 15056−15059.
(25) Chen, D.; Guan, Z.; Zhang, D.; Trotochaud, L.; Crumlin, E.; Nemsak, S.; Bluhm, H.; Tuller, H. L.; Chueh, W. C. Constructing a Pathway for Mixed Ion and Electron Transfer Reactions for O_2 Incorporation in $Pr_{0.1}Ce_{0.9}O_{2-x}$. *Nat. Catal.* **2020**, *3*, 116−124.
(26) Mamontov, E.; Egami, T. Structural Defects in a Nano-Scale Powder of CeO_2 Studied by Pulsed Neutron Diffraction. *J. Phys. Chem. Solids* **2000**, *61*, 1345−1356.
(27) Chen, J.; Arandiyan, H.; Gao, X.; Li, J. Recent Advances in Catalysts for Methane Combustion. *Catal. Surv. Asia* **2015**, *19*, 140−171.
(28) Grimaud, A.; Diaz-Morales, O.; Han, B.; Hong, W. T.; Lee, Y.-L.; Giordano, L.; Stoerzinger, K. A.; Koper, M. T. M.; Shao-Horn, Y. Activating Lattice Oxygen Redox Reactions in Metal Oxides to Catalyse Oxygen Evolution. *Nat. Chem.* **2017**, *9*, 457−465.
(29) Li, T.; Yao, Y.; Ko, B. H.; Huang, Z.; Dong, Q.; Gao, J.; Chen, W.; Li, J.; Li, S.; Wang, X.; Shahbazian-Yassar, R.; Jiao, F.; Hu, L. Carbon-Supported High-Entropy Oxide Nanoparticles as Stable Electrocatalysts for Oxygen Reduction Reactions. *Adv. Funct. Mater.* **2021**, *31*, 2010561.
(30) Lee, S. S.; Zhu, H.; Contreras, E. Q.; Prakash, A.; Puppala, H. L.; Colvin, V. L. High Temperature Decomposition of Cerium Precursors to Form Ceria Nanocrystal Libraries for Biological Applications. *Chem. Mater.* **2012**, *24*, 424−432.
(31) Elias, J. S.; Risch, M.; Giordano, L.; Mansour, A. N.; Shao-Horn, Y. Structure, Bonding, and Catalytic Activity of Monodisperse, Transition-Metal-Substituted CeO_2 Nanoparticles. *J. Am. Chem. Soc.* **2014**, *136*, 17193−17200.
(32) Binder, A. J.; Toops, T. J.; Unocic, R. R.; Parks, J. E.; Dai, S. Low-Temperature CO Oxidation over a Ternary Oxide Catalyst with High Resistance to Hydrocarbon Inhibition. *Angew. Chem. Int. Ed.* **2015**, *54*, 13263−13267.
(33) Lu, J.; Wang, J.; Zou, Q.; He, D.; Zhang, L.; Xu, Z.; He, S.; Luo, Y. Unravelling the Nature of the Active Species as Well as the Doping Effect over Cu/Ce-Based Catalyst for Carbon Monoxide Preferential Oxidation. *ACS Catal.* **2019**, *9*, 2177−2195.
(34) Kim, K.; Han, J. W. Mechanistic Study for Enhanced CO Oxidation Activity on (Mn,Fe) Co-Doped CeO_2 (111). *Catal. Today* **2017**, *293*−*294*, 82−88.
(35) Chen, H.; Jie, K.; Jafta, C. J.; Yang, Z.; Yao, S.; Liu, M.; Zhang, Z.; Liu, J.; Chi, M.; Fu, J.; Dai, S. An Ultrastable Heterostructured Oxide Catalyst Based on High-Entropy Materials: A New Strategy toward Catalyst Stabilization via Synergistic Interfacial Interaction. *Appl. Catal. B Environ.* **2020**, *276*, 119155.
(36) McCormick, C. R.; Schaak, R. E. Simultaneous Multication Exchange Pathway to High-Entropy Metal Sulfide Nanoparticles. *J. Am. Chem. Soc.* **2021**, *143*, 1017−1023.
(37) Chen, Y.; Zhan, X.; Bueno, S. L. A.; Shafei, I. H.; Ashberry, H. M.; Chatterjee, K.; Xu, L.; Tang, Y.; Skrabalak, S. E. Synthesis of Monodisperse High Entropy Alloy Nanocatalysts from Core@shell Nanoparticles. *Nanoscale Horiz.* **2021**, *6*, 231−237.
(38) Zhang, F.; Jin, Q.; Chan, S. W. Ceria Nanoparticles: Size, Size Distribution, and Shape. *J. Appl. Phys.* **2004**, *95*, 4319−4326.
(39) Ma, R.; Zhang, S.; Wen, T.; Gu, P.; Li, L.; Zhao, G.; Niu, F.; Huang, Q.; Tang, Z.; Wang, X. A Critical Review on Visible-Light-Response CeO_2-Based Photocatalysts with Enhanced Photooxidation of Organic Pollutants. *Catal. Today* **2019**, *335*, 20−30.
(40) Kümmerle, E. A.; Heger, G. The Structures of C−$Ce_2O_{3+\delta}$, Ce_7O_{12}, and $Ce_{11}O_{20}$. *J. Solid State Chem.* **1999**, *147*, 485−500.
(41) Oses, C.; Toher, C.; Curtarolo, S. High-Entropy Ceramics. *Nat. Rev. Mater.* **2020**, *5*, 295−309.
(42) Taniguchi, T.; Watanabe, T.; Sugiyama, N.; Subramani, A. K.; Wagata, H.; Matsushita, N.; Yoshimura, M. Identifying Defects in Ceria-Based Nanocrystals by UV Resonance Raman Spectroscopy. *J. Phys. Chem. C* **2009**, *113*, 19789−19793.
(43) Wu, Z.; Li, M.; Howe, J.; Meyer, H. M.; Overbury, S. H. Probing Defect Sites on CeO_2 Nanocrystals with Well-Defined Surface Planes by Raman Spectroscopy and O_2 Adsorption. *Langmuir* **2010**, *26*, 16595−16606.
(44) Holder, C. F.; Schaak, R. E. Tutorial on Powder X-Ray Diffraction for Characterizing Nanoscale Materials. *ACS Nano* **2019**, *13*, 7359−7365.
(45) Schmitt, R.; Nenning, A.; Kraynis, O.; Korobko, R.; Frenkel, A. I.; Lubomirsky, I.; Haile, S. M.; Rupp, J. L. M. A Review of Defect Structure and Chemistry in Ceria and Its Solid Solutions. *Chem. Soc. Rev.* **2020**, *49*, 554−592.
(46) Dimucci, I. M.; Lukens, J. T.; Chatterjee, S.; Carsch, K. M.; Titus, C. J.; Lee, S. J.; Nordlund, D.; Betley, T. A.; MacMillan, S. N.; Lancaster, K. M. The Myth of d8 Copper(III). *J. Am. Chem. Soc.* **2019**, *141*, 18508−18520.
(47) Nakamatsu, H.; Mukoyama, T.; Adachi, H. Ionic and Covalent Bonds in CeO_2 Crystal. *Chem. Phys. Lett.* **1995**, *247*, 168−172.
(48) Wang, W. W.; Yu, W. Z.; Du, P. P.; Xu, H.; Jin, Z.; Si, R.; Ma, C.; Shi, S.; Jia, C. J.; Yan, C. H. Crystal Plane Effect of Ceria on Supported Copper Oxide Cluster Catalyst for CO Oxidation: Importance of Metal-Support Interaction. *ACS Catal.* **2017**, *7*, 1313−1329.
(49) Luo, S.; Li, M.; Fung, V.; Sumpter, B. G.; Liu, J.; Wu, Z.; Page, K. New Insights into the Bulk and Surface Defect Structures of Ceria Nanocrystals from Neutron Scattering Study. *Chem. Mater.* **2021**, *33*, 3959−3970.
(50) Zhang, J.; Yan, J.; Calder, S.; Zheng, Q.; McGuire, M. A.; Abernathy, D. L.; Ren, Y.; Lapidus, S. H.; Page, K.; Zheng, H.; Freeland, J. W.; Budai, J. D.; Hermann, R. P. Long-Range Antiferromagnetic Order in a Rocksalt High Entropy Oxide. *Chem. Mater.* **2019**, *31*, 3705−3711.
(51) Jiang, B.; Bridges, C. A.; Unocic, R. R.; Pitike, K. C.; Cooper, V. R.; Zhang, Y.; Lin, D.-Y.; Page, K. Probing the Local Site Disorder and Distortion in Pyrochlore High-Entropy Oxides. *J. Am. Chem. Soc.* **2021**, *143*, 4193−4204.
(52) Santodonato, L. J.; Zhang, Y.; Feygenson, M.; Parish, C. M.; Gao, M. C.; Weber, R. J. K.; Neuefeind, J. C.; Tang, Z.; Liaw, P. K. Deviation from High-Entropy Configurations in the Atomic Distributions of a Multi-Principal-Element Alloy. *Nat. Commun.* **2015**, *6*, 5964.
(53) Billinge, S. J. L. Nanoscale Structural Order from the Atomic Pair Distribution Function (PDF): There's Plenty of Room in the Middle. *J. Solid State Chem.* **2008**, *181*, 1695−1700.
(54) Liu, H.; Liu, H.; Lapidus, S. H.; Meng, Y. S.; Chupas, P. J.; Chapman, K. W. Sensitivity and Limitations of Structures from X-Ray and Neutron-Based Diffraction Analyses of Transition Metal Oxide Lithium-Battery Electrodes. *J. Electrochem. Soc.* **2017**, *164*, A1802−A1811.
(55) Marchbank, H. R.; Clark, A. H.; Hyde, T. I.; Playford, H. Y.; Tucker, M. G.; Thompsett, D.; Fisher, J. M.; Chapman, K. W.; Beyer, K. A.; Monte, M.; Longo, A.; Sankar, G. Structure of Nano-Sized CeO_2 Materials: Combined Scattering and Spectroscopic Investigations. *ChemPhysChem* **2016**, *17*, 3494−3503.

https://doi.org/10.1021/acscentsci.2c00340
ACS Cent. Sci. 2022, 8, 1081−1090

(56) Liu, J.; Olds, D.; Peng, R.; Yu, L.; Foo, G. S.; Qian, S.; Keum, J.; Guiton, B. S.; Wu, Z.; Page, K. Quantitative Analysis of the Morphology of {101} and {001} Faceted Anatase TiO_2 Nanocrystals and Its Implication on Photocatalytic Activity. *Chem. Mater.* **2017**, *29*, 5591−5604.
(57) Wilkens, H.; Schuckmann, O.; Oelke, R.; Gevers, S.; Schaefer, A.; Bäumer, M.; Zoellner, M. H.; Schroeder, T.; Wollschläger, J. Stabilization of the Ceria *t*-Phase (Ce_7O_{12}) Surface on Si(111). *Appl. Phys. Lett.* **2013**, *102*, 111602.
(58) Krcha, M. D.; Janik, M. J. Challenges in the Use of Density Functional Theory to Examine Catalysis by M-Doped Ceria Surfaces. *Int. J. Quantum Chem.* **2014**, *114*, 8−13.
(59) Sun, Y.; Dai, S. High-Entropy Catalysts: Supremacy of Diversity. *Chem. Catal* **2021**, *1*, 490−492.
(60) Fu, Q.; Li, W.-X.; Yao, Y.; Liu, H.; Su, H.-Y.; Ma, D.; Gu, X.-K.; Chen, L.; Wang, Z.; Zhang, H.; Wang, B.; Bao, X. Interface-Confined Ferrous Centers for Catalytic Oxidation. *Science* **2010**, *328*, 1141−1144.
(61) Fu, Q.; Yang, F.; Bao, X. Interface-Confined Oxide Nanostructures for Catalytic Oxidation Reactions. *Acc. Chem. Res.* **2013**, *46*, 1692−1701.
(62) Bao, Z.; Fung, V.; Moon, J.; Hood, Z. D.; Rochow, M.; Kammert, J.; Polo-Garzon, F.; Wu, Z. Revealing the Interplay between "Intelligent Behavior" and Surface Reconstruction of Non-Precious Metal Doped $SrTiO_3$ Catalysts during Methane Combustion. *Catal. Today* **2022**, DOI: 10.1016/j.cattod.2022.03.012.
(63) Li, Y.; Lin, L.; Gao, L.; Mu, R.; Fu, Q.; Bao, X. Predominance of Subsurface and Bulk Oxygen Vacancies in Reduced Manganese Oxide. *J. Phys. Chem. C* **2021**, *125*, 7990−7998.
(64) Chakhalian, J.; Millis, A. J.; Rondinelli, J. Whither the Oxide Interface. *Nat. Mater.* **2012**, *11*, 92−94.

https://doi.org/10.1021/acscentsci.2c00340
ACS Cent. Sci. 2022, 8, 1081−1090